ORIGINAL PAPER

Structural, morphological, spectroscopic, and electrochemical properties of Cr doped ZnAl$_2$O$_4$

K. Kiran Kumar[1] · T. Suresh Kumar[1] · B. Ravinder Reddy[2] · Ch. Shilpa Chakra[3] · K. Praveena[4] · S. Katlakunta[1]

Abstract

The $ZnAl_{2-x}Cr_xO_4$ ($x = 0.0–0.1$) ceramics were synthesized using microwave-hydrothermal method. The as synthesized powders were sintered at 1250 °C/4 h. All samples exhibit a cubic crystal structure and belong to Fd-3m space group. The lattice constant (a) increased from 8.085 Å ($x = 0.0$) to 8.128 Å ($x = 0.04$) and decreased for higher concentrations. The Fourier transform infrared spectra (FTIR) show tetrahedral and octahedral absorption bands in the region, 400 - 480 cm^{-1} and 480 – 682 cm^{-1}, respectively. The X-ray photoelectron spectroscopy confirmed the valence states of Zn, Al, Cr, and O. The UV-vis spectra reveal a red shift with Cr^{3+} doping, reducing the bandgap energy (E_g) from 3.66 eV ($x = 0.02$) to 3.39 eV ($x = 0.10$). The electrochemical performance of the present samples was investigated using cyclic voltammetry (CV) and galvanostatic charge/discharge (GDC). The sample $x = 0.10$ exhibits high specific capacity of 143.671 F/g at a scan rate 5 mV/s. Therefore, the present samples may be useful for energy storage devices.

Graphical Abstract

The tauc plots for $x = 0.0–0.10$ samples. The UV-vis spectra reveal a red shift with Cr^{3+} doping, reducing the bandgap energy (E_g) from 3.66 eV ($x = 0.02$) to 3.39 eV ($x = 0.10$).
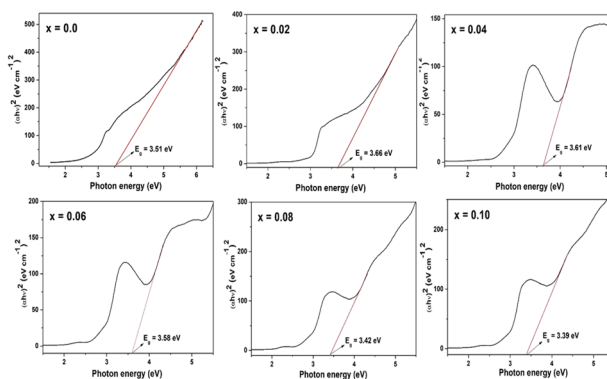
Keywords ZnAl$_2$O$_4$ · Nanoparticles · XPS · Energy band gap · Specific capacitance

✉ S. Katlakunta
sadhana@osmania.ac.in

1 Department of Physics, University College of Science, Saifabad, Osmania University, Hyderabad 500004, India

2 Department of Physics, University College of Science, Osmania University, Hyderabad 500007, India

3 Centre for Nano Science and Technology, Jawaharlal Nehru Technological University, Hyderabad, Telangana, India

4 Department of Physics, Palamuru University, Mahabubnagar, Telangana, India

Highlights

- The $ZnAl_{2-x}Cr_xO_4$ ($x = 0.0$–0.1) ceramics were synthesized using microwave-hydrothermal method.
- The UV-vis spectra reveal a red shift with Cr^{3+} doping, reducing the bandgap energy (E_g) from 3.66 eV ($x = 0.02$) to 3.39 eV ($x = 0.10$).
- The sample $x = 0.10$ exhibits high specific capacity of 143.671 F/g at a scan rate 5 mV/s.

1 Introduction

Recently, supercapacitors have gained attention due to their long life cycle, high power density, and flexibility as traditional dielectric capacitors and energy units [1, 2]. Researchers are exploring supercapacitors with high energy density and greater electricity storage capability to bridge the gap between batteries and capacitors. Supercapacitors can store energy through non-Faradaic mechanisms in electrical double layer capacitors and electrostatic methods in pseudo-capacitors [3, 4]. Therefore, nanomaterials exhibit superior characteristics over their bulk counterparts [5]. Compared to carbon based nanomaterials, inorganic metal oxides offer opportunities for tailor-made properties [5]. Because of their extremely narrow band gap and low cost, spinel-type metal oxides have drawn more attention than many other metal oxides [6]. The spinel-structured material, with its octahedral and tetrahedral voids, plays a crucial role in photocatalytic and electrochemistry applications [7]. A broad variety of areas utilize $ZnAl_2O_4$ nanoparticles due to their exceptional properties. These fields include photocatalysis, sensors, high temperature ceramics, dielectric materials, magnetics, electrode materials, opto-electronics, and dosimetry [8–11]. Researchers reported the optical band gap of spinel $ZnAl_2O_4$, a direct band gap semiconductor, to be between 3.8 and 3.9 eV [12].

Zinc aluminate ($ZnAl_2O_4$) exhibits a cubic structure and belongs to the space group Fd-3m. The spinel structure of $ZnAl_2O_4$ contains cations Zn^{2+} and Al^{3+}, which occupy tetrahedral and octahedral sites, respectively. Thermodynamic stability of these cations is compromised by the movement of Zn^{2+} and Al^{3+} cations between sites, resulting in an inverted spinel with all Zn^{2+} ions in the octahedral sites [13]. Reports indicate that spinels doped with transition metals excel in electrocatalysis. $ZnAl_2O_4$ is a suitable material for electrocatalytic applications due to its high redox activity and stability. Thirumala Rao et al. used hydrothermal technique to synthesize $ZnAl_2O_4$ for supercapacitor applications. Spinel $ZnAl_2O_4$ exhibits a specific capacitance of 260.4 $mAhg^{-1}$ and a columbic effectiveness of 98% over 500 cycles [14]. Zinc aluminate with rare earth doping, such as Eu^{3+}, Dy^{3+}, Tb^{3+}, and Ce^{3+}, enhanced their structural, optical and luminescent properties. However, because of the high cost of rare earth elements, transition elements have gained popularity as substitutes. Unlike rare earth elements, transition elements can occupy both octahedral and tetrahedral sites in the crystals due to valence states [15–18]. Researchers have used a variety of rare earth metal ions and transition metal ions as dopants. Due to its comparable ionic radii to rare earth ions, the $ZnAl_2O_4$ host material commonly uses the Cr^{3+} ion as a dopant [19].

Various synthesis methods were used to prepare $ZnAl_2O_4$, including solid-state method [20, 21], hydrothermal synthesis [22, 23], and the sol-gel method [24, 25]. The solid-state synthesis needs the physical mixing of the various precursors, followed by sintering [26]. It also requires high temperature sintering and long hours. It is difficult to control the particle size and maintain homogeneity [27]. The chemical methods are advantageous because of their ease of preparation, high yields, low sintering temperatures and times, homogeneity, and so on. Miron, Grozescy, and Hong et al. [28, 29] reported the hydrothermal synthesis of Cr^{3+} doped $ZnAl_2O_4$, with synthesis times ranging from 16 h to 96 h. Motloung et al. [30] described the sol-gel synthesis of Cr^{3+} doped $ZnAl_2O_4$. Dong et al. [31] synthesized Cr-doped $ZnAl_2O_4$ using an electrospinning method. Samvit Menon et al. reported the synthesis of Cr doped $ZnAl_2O_4$ using the co-precipitation method [19].

Therefore, the present investigation employs the microwave-hydrothermal method to synthesize Cr doped $ZnAl_2O_4$ nanoparticles. The influence of Cr^{3+} on the structural, spectroscopic, and electrochemical properties was investigated to find a suitable material for supercapacitor applications. The Cr doped $ZnAl_2O_4$ samples were characterized using X-ray diffraction (XRD), field emission scanning electron microscopy (FESEM), Fourier transform infrared spectroscopy (FTIR), UV-Vis spectrometer, X-ray photoelectron spectroscopy (XPS), and an electrochemical analyzer, and all the results are explained in detail.

2 Experimental method

The nanopowders of $ZnAl_{2-x}Cr_xO_4$ ($x = 0.0$–0.1) were synthesized using the microwave-hydrothermal method. A similar synthesis procedure was reported elsewhere [22, 32, 33]. Analytical-grade chemicals $Zn(NO_3)_2.6H_2O$, $Al(NO_3)_3.9H_2O$, and $Cr(NO_3)$ were used in the synthesis. For the synthesis of $ZnAl_2O_4$, the zinc nitrate and aluminum nitrate were weighed according to the stoichiometric ratio,

dissolved in deionized water, and stirred well to obtain a clear solution. A drop wise NaOH solution was added to the clear solution to get a pH of ~11. The precipitate was then transferred into a tetrafluorometoxil (TFM) reaction vessel which was then mounted on the turntable in the Microwave Accelerated Reaction System (Model MARS-5, CEM Corp. Mathews, NC) for microwave treatment at 200 °C for 60 min. It operates at 2.45 GHz with 1200 ± 50 W of power and can attain a maximum pressure of 800 psi and a temperature of 240 °C. After treatment, the product was centrifuged and repeatedly washed it with deionized water until the pH reached neutral, and then filtered it. The powders were dried overnight at 80 °C in an oven. The dried powders were finally sintered at 1250 °C for 4 h in a muffle furnace.

The X-ray diffraction patterns were recorded using X-ray diffractometer (Phillips PANanalytical) that used Cu-Kα radiation ($\lambda = 1.5406$), a scanning range of $2\theta = 20°–80°$, and a scan rate of 1°/min at 40 kV and 30 mA. The field emission scanning electron microscope (FESEM, FEI Quanta 200) in conjunction with energy dispersive spectra (EDS), were used for microstructural study and elemental analysis, respectively. The ImageJ software was used to analyze the microstructure of all the samples, which included grain size distribution, histograms, and average grain size. The Fourier transform infrared (FTIR) spectra were recorded in the mid-IR range of 4000–400 cm^{-1} at a resolution of 4 cm^{-1} using Brucker Tensor 27 spectrometer. The absorbance spectra were collected between 200 and 900 nm using a UV-visible spectrophotometer (Shimadzu, UV-1800) at a resolution of 1 nm. A 10 kV and 10 mA Shimadzu ESCA-3400 spectrophotometer (Kyoto, Japan) was used for the monochromatic Mg-Kα X-ray source (1253.6 eV) measurements.

An electrochemical analysis was conducted using the Metrohm Autolab PGSTA302N instrument and NOVA 2.0.2 software. The analysis involved techniques such as cyclic voltammetry (CV) and galvanostatic charge/discharge (GDC), and a three-electrode system was utilized with Ag/AgCl as the reference electrode and Pt as the counter electrode. The working electrodes were prepared using current samples as the active material (80%), activated carbon (10%), and polyvinylidene fluoride (PVDF) (10%), which acts as the cathode. PVDF possesses remarkable chemical resistance to electrodes, a remarkable temperature tolerance, and an organic binder, enabling it to endure a diverse array of weather conditions without succumbing to deterioration. Activated carbon was used as a solvent to enhance the chemically active surface area and minimize the adsorbent between the electrode and electrolyte, thus expanding its effectiveness. Apply a layer of PVDF and activated carbon compound as a thick slurry onto a 1 by 1 centimeter Ni foam substrate. Heat the coated substrate in an oven at 80 °C for 12 h. The fabricated samples are used for supercapacitor applications.

3 Results and discussion

3.1 X-ray Diffractograms (XRD)

The X-ray diffractograms of $ZnAl_{2-x}Cr_xO_4$ ($x = 0.0–0.10$) samples are shown in Fig. 1. All the diffraction peak positions were compared to JCPDF card no: 74-1138 and all the peaks were matched with spinel $ZnAl_2O_4$. The characteristic peak (hkl:311) suggests that all the samples exhibit cubic structure with the space group Fd-3m. No impurity phases were observed in all the samples. The intensity of hkl: 311 increased with Cr doping for $x = 0.02$ and decreases for $x = 0.04$. For samples with $x > 0.04$, there is an increase in intensity. The variation in the intensity of the peak with respect to doping is that Cr ions are incorporated nonhomogeneously into the host $ZnAl_2O_4$ matrix due to the difference in the ionic radius and chemical oxidation states [34]. It is obvious that Cr^{3+} ions enter the crystal lattice of $ZnAl_2O_4$. In general, Cr^{3+} ions occupy octahedral sites because they replace Al^{3+} ions in the $ZnAl_2O_4$ host, however, depending on the Cr doping concentration, synthesis circumstances, sintering temperature, and particle size, Cr may occupy both tetrahedral and octahedral sites [31]. Using the conventional Archimedes method, the bulk densities (d_b) were calculated for all of the samples. The strain (ε) and an average crystallite size ($<D>$) are determined from the Williamson-Hall plot, as illustrated in Fig. 2. Table 1 shows the average crystallite size, lattice strain, lattice parameter (a), unit cell volume (V), X-ray density (d_x), bulk density (d_b) and percent of porosity ($\%P$).
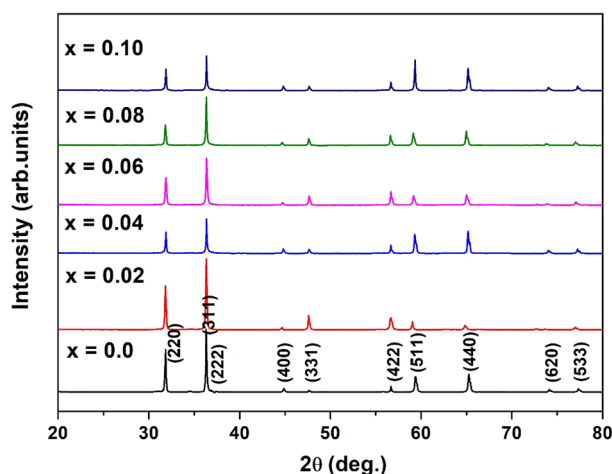

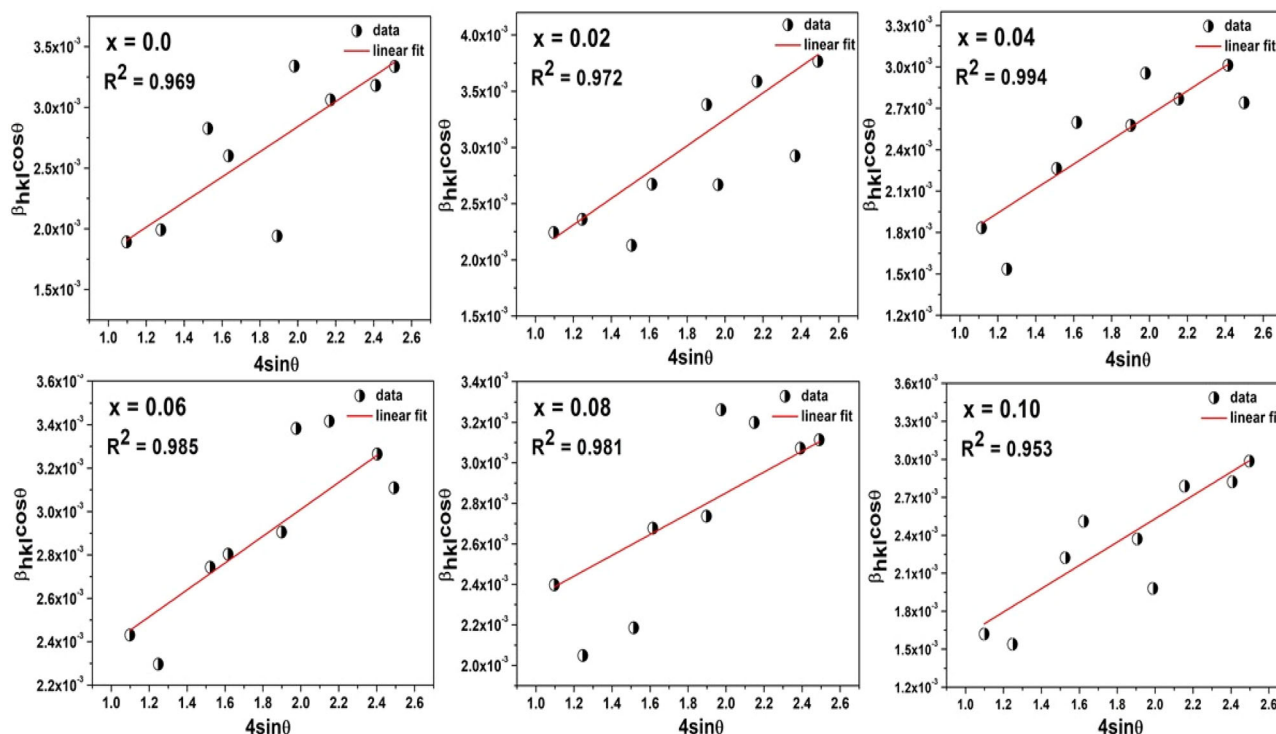**Fig. 1** X-ray diffraction patterns of $ZnAl_{2-x}Cr_xO_4$ ($x = 0.0$ to 0.10)

Fig. 2 Williamson-Hall plots for Cr doped $ZnAl_2O_4$

Table 1 Structural parameters: lattice constant (a), unit cell volume (V), X-ray density (d_x), bulk density (d_b), percentage of porosity (%P), crystallite size < D >, lattice strain (ε) and grain size

x	a (Å)	V(Å^3)	d_x(g/cm^3)	d_b(g/cm^3)	%P	<D> (nm)	ε (x10^{-3})	Grain size (nm)
0.0	8.085	528.494	3.401	3.252	4	70	2.71	84
0.02	8.088	529.082	3.410	3.126	8	126	1.06	95
0.04	8.128	536.971	3.372	3.042	9	86	1.64	113
0.06	8.121	535.585	3.393	3.140	7	64	2.21	132
0.08	8.115	534.398	3.413	3.315	2	85	2.58	169
0.10	8.104	532.228	3.440	3.281	4	80	2.67	198

Figure 3 shows the variation of lattice constant (a) in response to Cr doping (x). With Cr doping, a is increased from 8.085 Å ($x = 0.0$) to 8.128 Å ($x = 0.04$) and then decreased to 8.104 Å ($x = 0.10$). The substitution the smaller ionic radii of Al^{3+} (0.53 Å) with higher ionic radii of Cr^{3+} (0.63 Å) results in increase in the lattice constant (a) [28, 34]. For higher substitution ($x > 0.04$) of Cr^{3+} ions for Al^{3+} ions at octahedral sites and Zn^{2+} (ionic radii of 0.74 Å) ions at tetrahedral sites, the drop in a occurs [30]. The unit cell volume (V) varies in the same manner as the lattice constant, suggests that Cr^{3+} is soluble in the $ZnAl_2O_4$ lattice. The X-ray density (d_x) of samples varied non linearly with Cr doping, as the density of the sample depends on the molar masses of Zn (65.4 g/mol), Al (27 g/mol), and Cr (51.996 g/mol) [35]. It is observed from Table 1 that the bulk density (d_b) varied non-linearly with x. Variations in
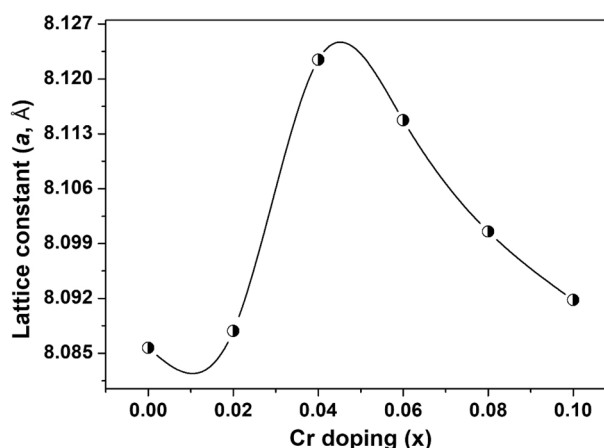

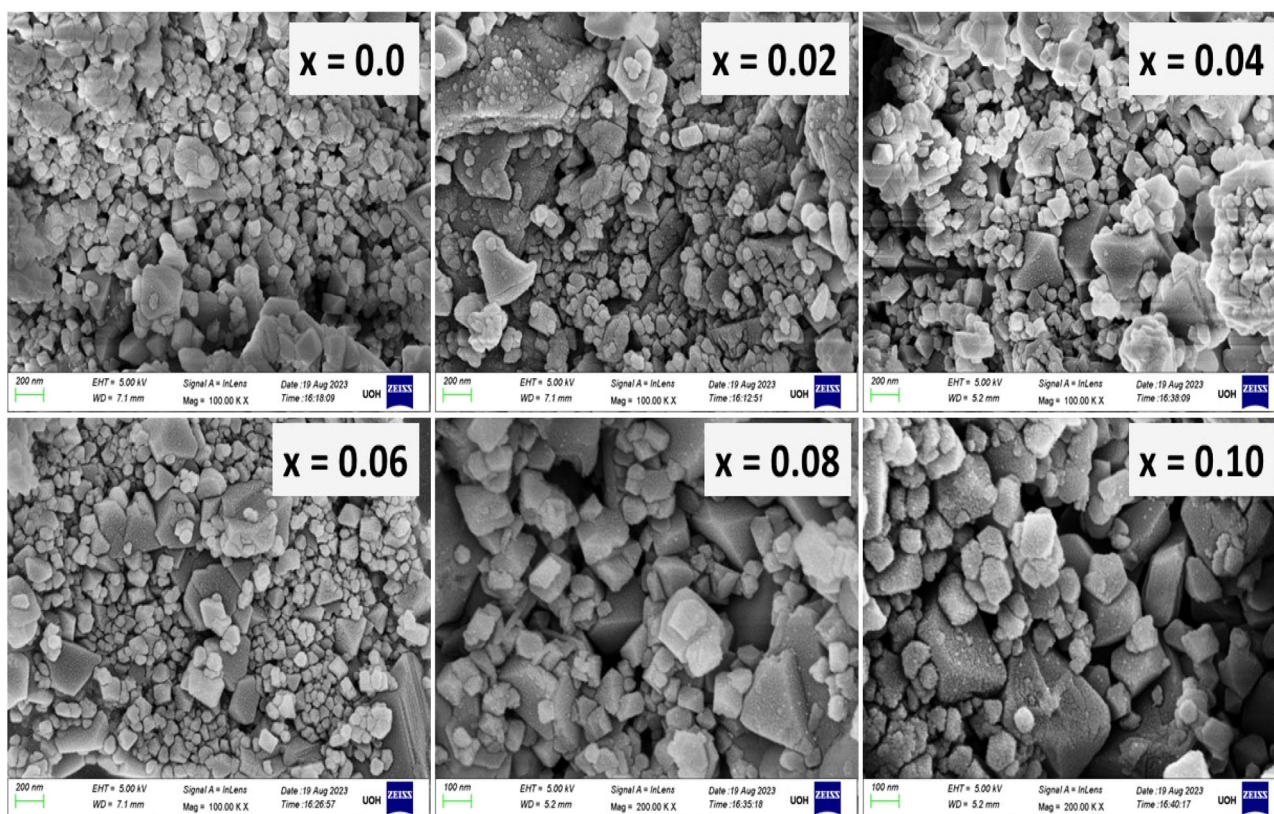Fig. 3 The Variations in the lattice constant (a) with respect to Cr doping (x)

Fig. 4 FESEM images for $ZnAl_{2-x}Cr_xO_4$ ($x = 0.0$ to 0.10) samples

the percentage of porosity (%P) with doping concentration is may be due to defects. The rise in lattice strain (ε) could be attributed to the generation of oxygen vacancies on the nanoparticle surfaces [36].

3.2 Field emission scanning electron microscopy (FESEM)

Figure 4 displays FESEM images of $ZnAl_{2-x}Cr_xO_4$ (where x ranges from 0.0 to 0.10) samples. The images exhibit uneven morphology and irregular particles sizes distribution. The average grain size ($<D_g>$) was determined using Image J software. The grain size distribution histograms are presented in Fig. 5. The average grain size ($<D_g>$) values are in a range of 84 nm ($x = 0.0$) to 198 nm ($x = 0.10$) and the results are tabulated in Table 1. It is observed that the average grain size increased with Cr doping. The increase in grain size may be due to the presence of Van Der Waals force, coulomb force, or chemical bond cooperation between the nanoparticles [37]. Figure 6 represents the energy-dispersive X-ray spectroscopy (EDS) of the samples, revealing the presence of Zn, Al, Cr, and O elements. This observation suggests that the prepared samples are devoid of any impurities.

3.3 The FTIR spectroscopy

The FTIR spectra of Cr-doped $ZnAl_2O_4$ in the range of 400–4000 cm^{-1} are displayed in Fig. 7. The peaks corresponding to the wavenumbers of around 3311–3325 cm^{-1} and 1619–1639 cm^{-1} for all samples are associated with the stretching and bending vibrations of the hydroxyl groups of absorbed water [25, 26, 38]. The N-H bending vibrational modes were observed in a wavenumber range of 1473 to 1483 cm^{-1} [39]. Three absorption bands were identified at approximately 649 cm^{-1}, 544 cm^{-1}, and 497 cm^{-1} for $x = 0.0$. The formation of the spinel cubic phase is indicated by the presence of these three peaks. The two prominent bands at 649 cm^{-1} and 544 cm^{-1} represent the symmetric stretching vibrational modes of octahedral Al^{3+} ions caused by Al-O symmetric stretching. On the other hand, the band at 497 cm^{-1} corresponds to the symmetric stretching vibrations of tetrahedral ZnO_4 [40, 41]. Unlike the absorption bands seen at 497 cm^{-1} and 544 cm^{-1}, the intensity at 649 cm^{-1} is influenced by the doping parameter x. The observed change in intensity indicates the incorporation of Cr^{3+} ions into the spinel lattice, where they substitute Al^{3+} ions. The absorption bands below 497 cm^{-1} are attributed to the stretching modes of Zn-O [42, 43]. The band at 809 cm^{-1} is attributed to the symmetric stretching of octahedral Al^{3+}. The absorption at
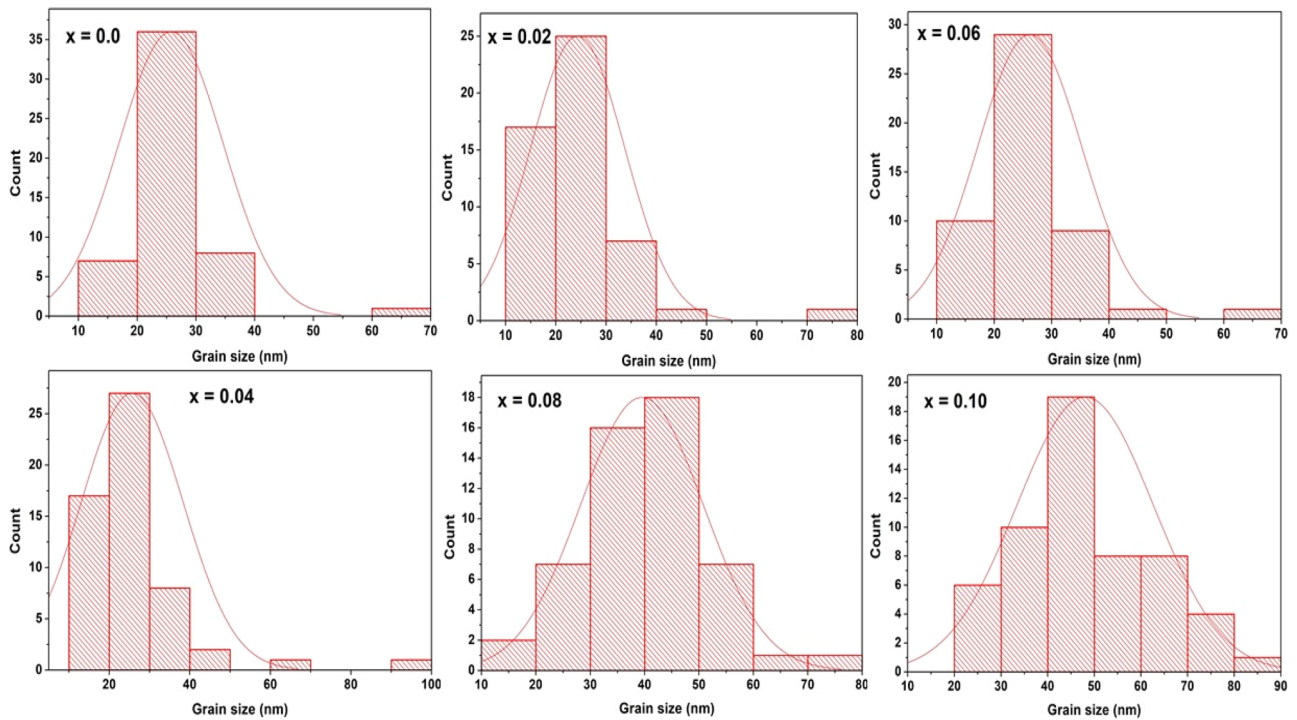
Fig. 5 Grain size distribution (histograms) for $ZnAl_{2-x}Cr_xO_4$ ($x = 0.0$ to 0.10)
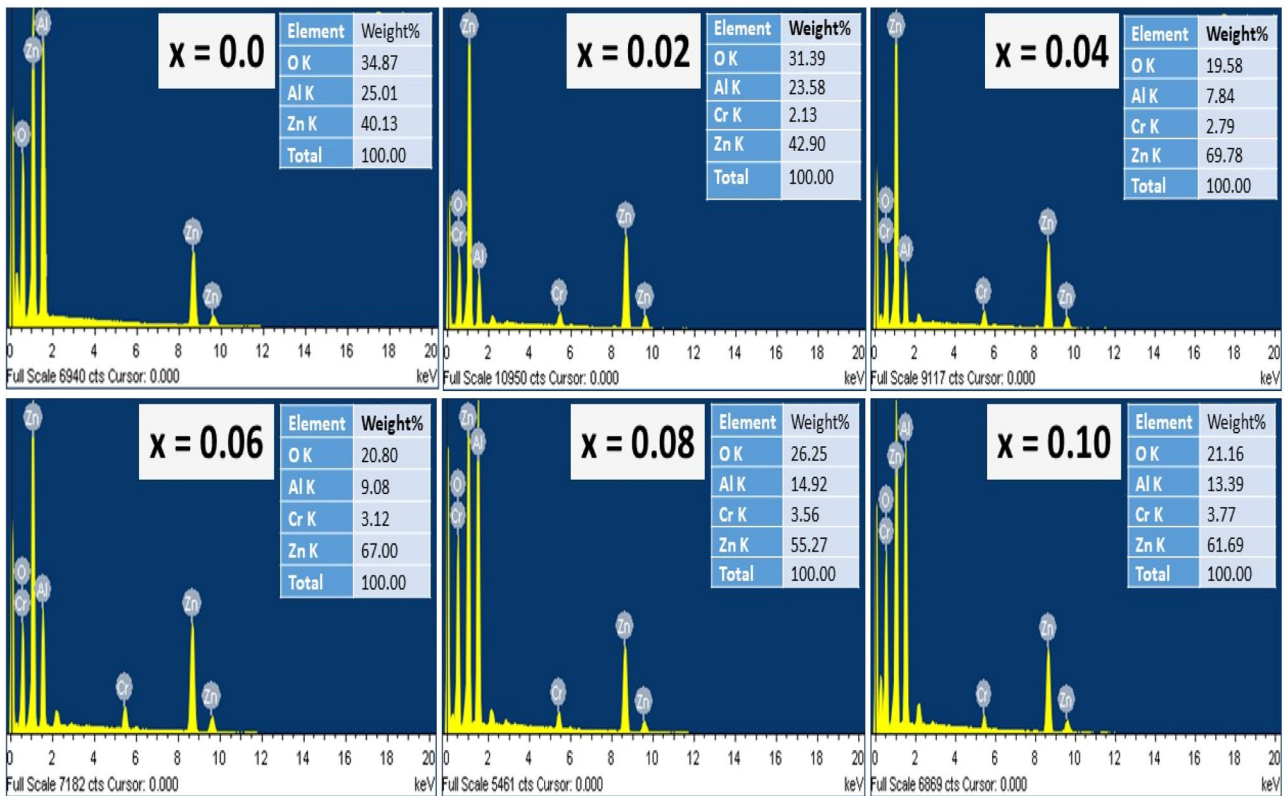

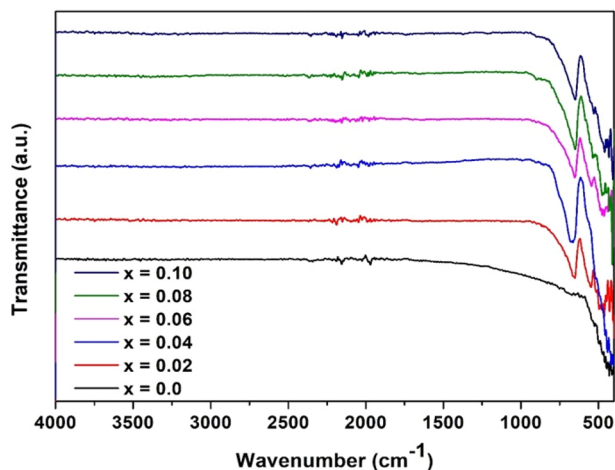Fig. 6 EDS images for $ZnAl_{2-x}Cr_xO_4$ ($x = 0.0$ to 0.10)

Fig. 7 The FTIR spectrum of $ZnAl_{2-x}Cr_xO_4$ ($x = 0.0$–0.10)

Fig. 8 UV-Vis absorbance spectra for $x = 0.0$–0.10 samples

$516\ cm^{-1}$ is indicative of the asymmetrical stretching mode of octahedral Al^{3+}. The presence of the $411\ cm^{-1}$ and $431\ cm^{-1}$ bands may be attributed to the tetrahedral Al^{3+} [44–46].

3.4 UV-Vis absorbance spectra

Figure 8 displays the ultraviolet-visible (UV-Vis) absorbance spectra of $ZnAl_{2-x}Cr_xO_4$ (where x ranges from 0.0 to 0.10) nanoparticles recorded in within the wavelength range of 200 nm to 800 nm. The absorption edge in the lower wavelength range (230–279 nm) may be caused by the lattice distortion resulting from the introduction of Cr at Al^{3+} sites [47, 48]. The absorption band at 230–279 nm may be due to the charge transfer transitions of the Cr ion [48]. But such an absorption band is absent for $x = 0.0$ [49] but clearly visible for Cr doped samples. The samples exhibit high absorbance at wavelengths 273 nm and 371 nm, which fall between the UV and visible region. According to the literature, the absorbance in the sample may be affected by several factors, such as impurity concentrations, thickness of the sample, dopant concentration, the band gap energy, the oxygen packing density, the molar volume density of the sample, and the size of the particle [50]. The different band gaps of all the samples were determined by employing tauc's plot and applying Equation [10, 51].

$$(\alpha h\nu) = (h\nu - E_g)^n$$

For direct band gap semiconductors, the optical band gap energy is denoted by E_g, the energy of an incident photon may be denoted by $h\nu$, the coefficient of absorption is denoted by $\alpha(\nu)$, the frequency of vibration is denoted by ν, and the value of n is equal to ½. The optical band gap E_g can be determined by extrapolating a straight line in the tauc plot of $h\nu$ vs $(\alpha h\nu)^2$.
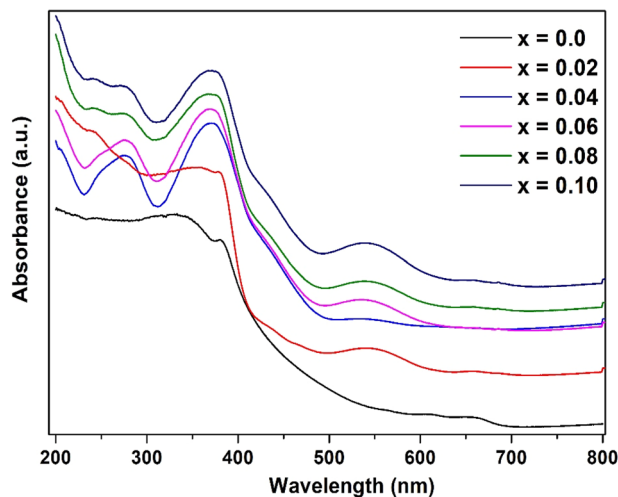
All samples exhibited two distinct absorption bands at 330–375 nm and 530–560 nm. There is a possibility that the absorption bands between 330 and 375 nm are caused by transitions from O-Al to tetrahedral sites ($^4A_2 \rightarrow {}^4T_1$). Absorption bands in the range of 530 to 560 nm are produced as a result of transitions ($^4A_2 \rightarrow {}^4T_1$) involving O-Al in octahedral sites [52]. This is because the $ZnAl_2O_4$ lattice contains Cr^{3+} spin permitted d - d transitions, which are responsible for these transitions [19, 53]. Figure 9 displays the tauc plots for $ZnAl_{2-x}Cr_xO_4$ ($x = 0.0$ -0.1). For $x = 0.0$, the band gap energy (E_g) is 3.51 eV, which is lower than the band gap of bulk $ZnAl_2O_4$ (3.8 eV) [12]. This difference may be owing to the quantum confinement limit [54]. With Cr^{3+} doping, the bandgap energy E_g decreased from 3.51 eV ($x = 0.0$) to 3.39 eV ($x = 0.10$) by exhibiting a red shift. The red shift is brought about by the sp-d interaction that takes place between band electrons and local electrons in the d-shell of the substituted cation. These interactions decrease the conduction band potential and increase the valence band potential, which ultimately results in a reduction in the band gap [37, 55].

3.5 X-ray photoelectron spectra (XPS)

The X-ray photoelectron (XPS) wide spectrum of $ZnAl_{2-x}Cr_xO_4$ ($x = 0.06$) is shown in Fig. 10a. The Cr 2p core level spectra for $x = 0.06$ can be seen in Fig. 10b. The Cr 2p spectrum is split into two main peaks, which are Cr $2p_{3/2}$ and Cr $2p_{1/2}$. These peaks have binding energies 575.77 eV (Cr^{3+}) and 584.39 eV (Cr^{3+}), respectively. In the octahedron, the Cr $2p_{3/2}$ peak corresponds to Cr ions, whereas in the tetrahedron, at Cr $2p_{1/2}$, there are only a few Cr ions. The core spectrum of Zn 2p can be seen in Fig. 10c. The two major peaks at 1047.19 eV and 1024.01 eV, are ascribed to Zn $2p_{1/2}$ and Zn $2p_{3/2}$, respectively. In addition to
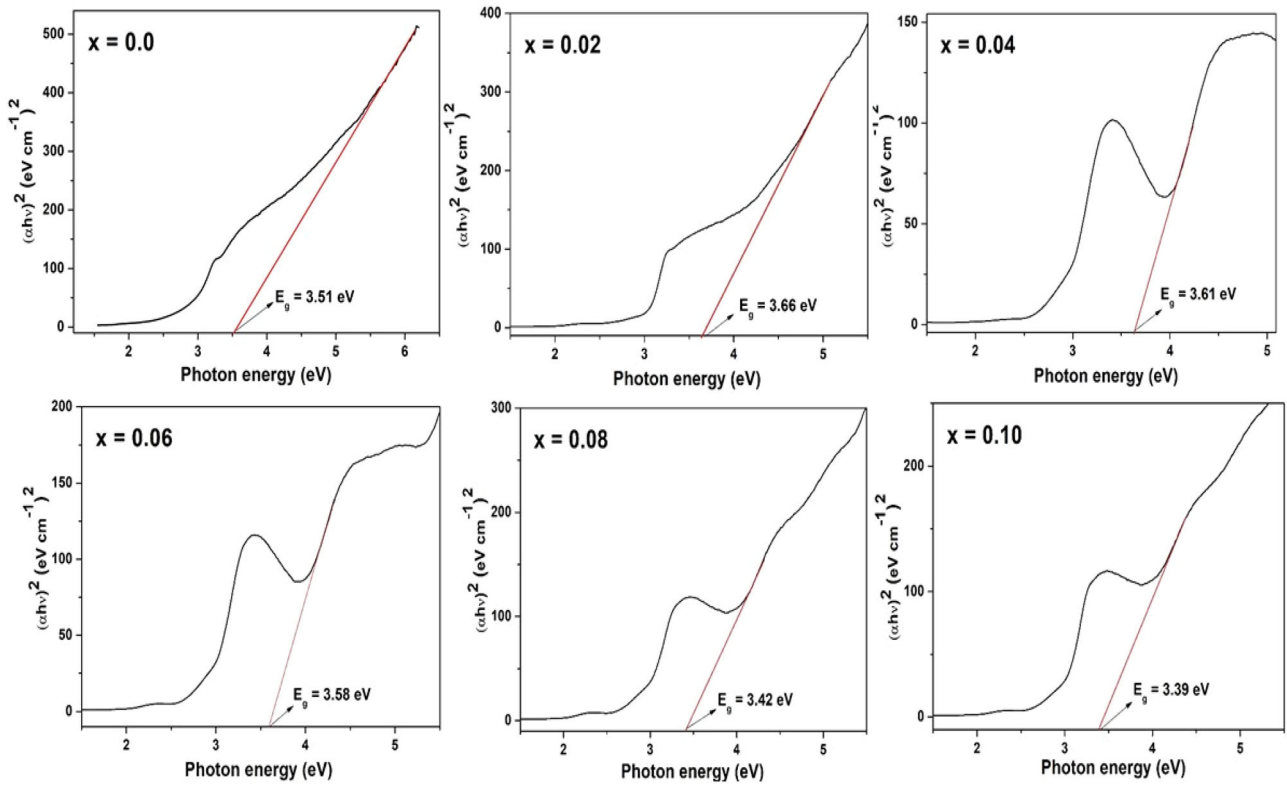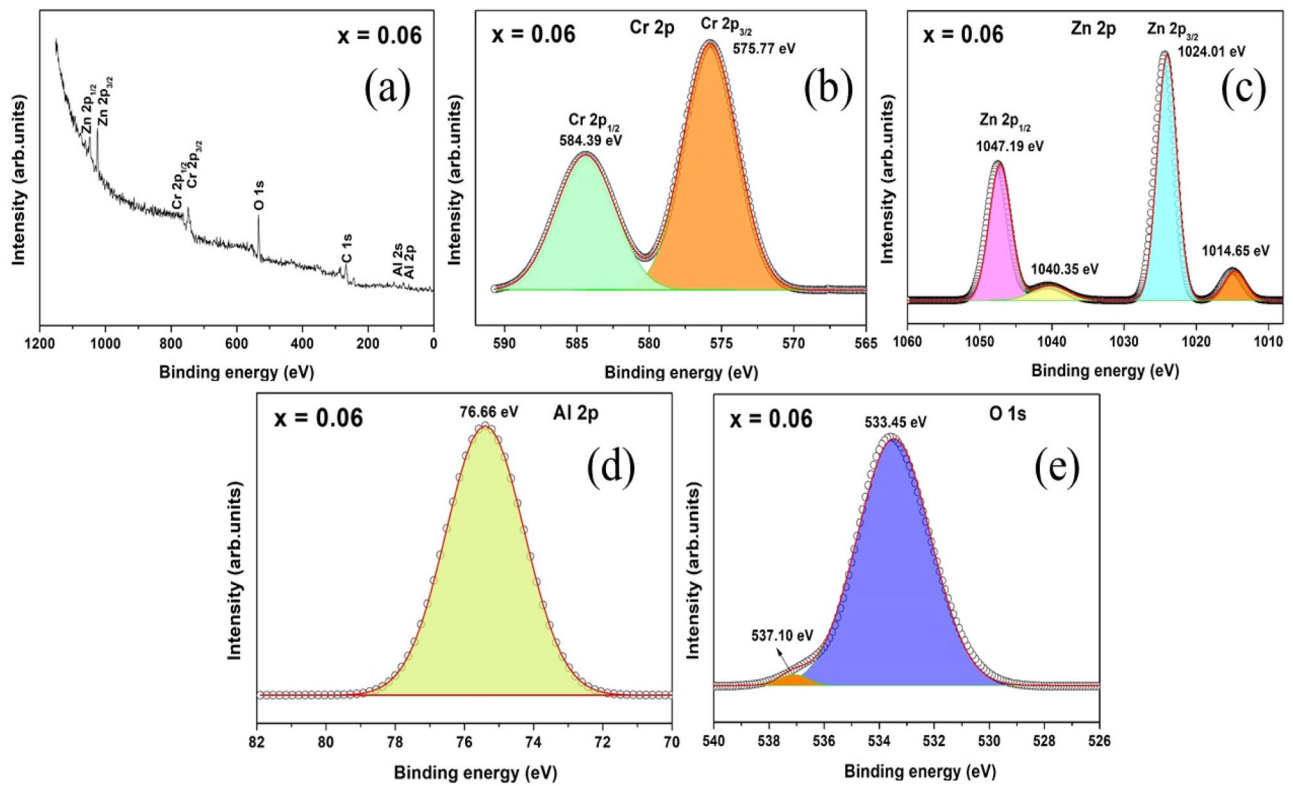
Fig. 9 Tauc plots for $x = 0.0$–0.10

Fig. 10 XPS spectra for samples $x = 0.06$ (**a**) wide spectra (**b**) Cr 2p (**c**) Zn 2p (**d**) Al 2p (**e**) O 1 s

these peaks, two peaks at 1014.65 eV and 1040.35 eV is present. The difference in energy between Zn $2p_{3/2}$ and Zn $2p_{1/2}$ is 23.18 eV, which confirms that Zn^{2+} is present in all samples. Figure 10d shows the core level Al 2p spectrum for $x = 0.06$. The binding energy at 76.66 eV confirms the presence of Al^{3+} in sample $x = 0.06$. The O 1 s spectra is deconvoluted and exhibits two peaks at binding energies

533.45 eV and 537.10 eV (shown in Fig. 10e). The peak at 533.45 eV is due to the oxygen vacancies present in the $ZnAl_2O_4$ lattice, and the peak at 537.01 eV is due to adsorbed oxygen on the surface of the sample [54].

3.6 Electrochemical properties

The cyclic voltammetry (CV) studies for $x = 0.0–0.10$ obtained in a 1 M KOH aqueous solution at 5 mV/s scan rate in the potential window of –0.1 V to 0.4 V are displayed in Fig. 11. An observed elevation in the scanning rate demonstrates a subtle shift in the potential values of the oxidation-reduction peaks [56]. The reduction peaks for all samples, ranging from $x = 0.0$ to $x = 0.10$, were obtained by conducting reverse/cathodic scans from 0.2 to 0.25 V. Conversely, the oxidation peaks were collected by doing forward/anodic scans from 0.3 to 0.35 V. The cyclic voltammetry (CV) curves provide convincing evidence of the Faradaic capacitive behavior [57], as a distinct pair of redox peaks is prominently observed for samples with $x = 0.0$ to 0.1. The observed variations in redox peaks in both the anode and cathode directions could potentially be attributed to the delayed migration of electrolyte ions, specifically OH- ions [58]. Figure 12 depicts the Galvanostatic Charge-Discharge (GCD) curve for all the samples.
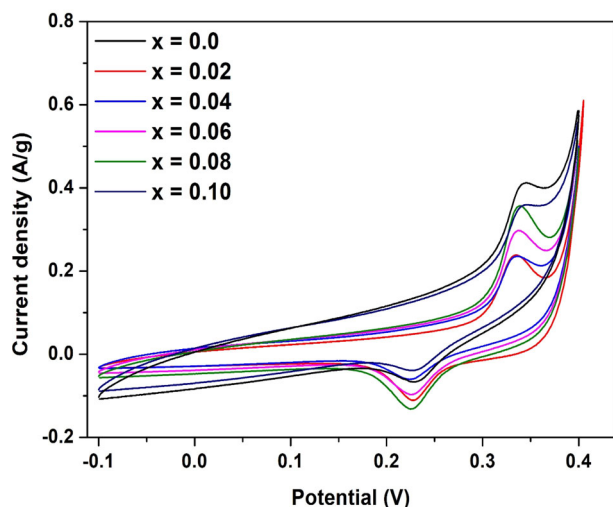

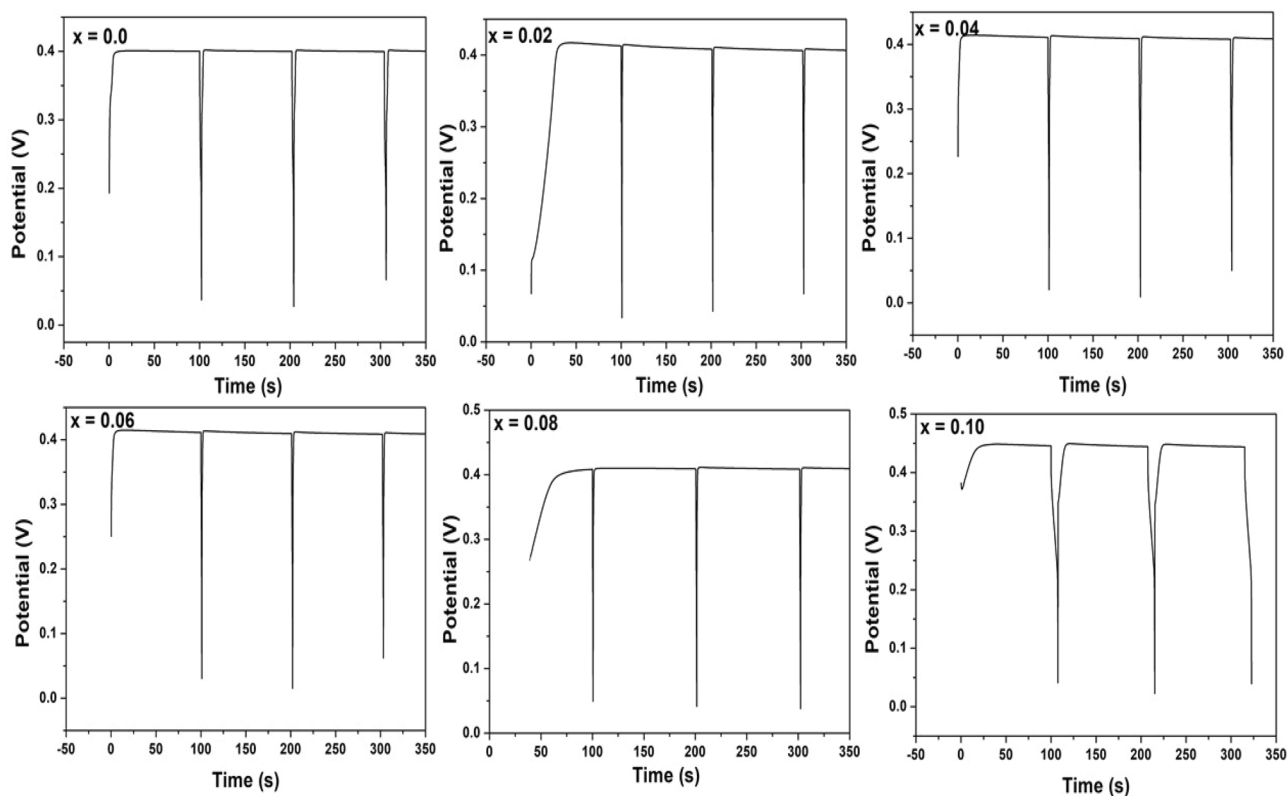**Fig. 11** Cyclic voltammetry (CV) curves for $x = 0.0–0.10$ recorded in 1 M KOH aqueous solution with 5 mV/s rate of scan

Fig. 12 Galvanostatic charge-discharge (GCD) curved for all the samples, $x = 0.0–0.10$

Table 2 The data of specific capacitance (C_{sp}), energy density (E_d) and power density (P_d) for $x = 0.0$–0.10

x	C_{sp} (F/g)	E_d (Wh/kg)	P_d (W/kg)
0.0	70.286	2.439	15.790
0.02	79.731	2.767	44.514
0.04	84.113	2.919	24.562
0.06	95.499	3.315	53.718
0.08	106.815	3.707	58.546
0.10	143.671	4.987	8.357
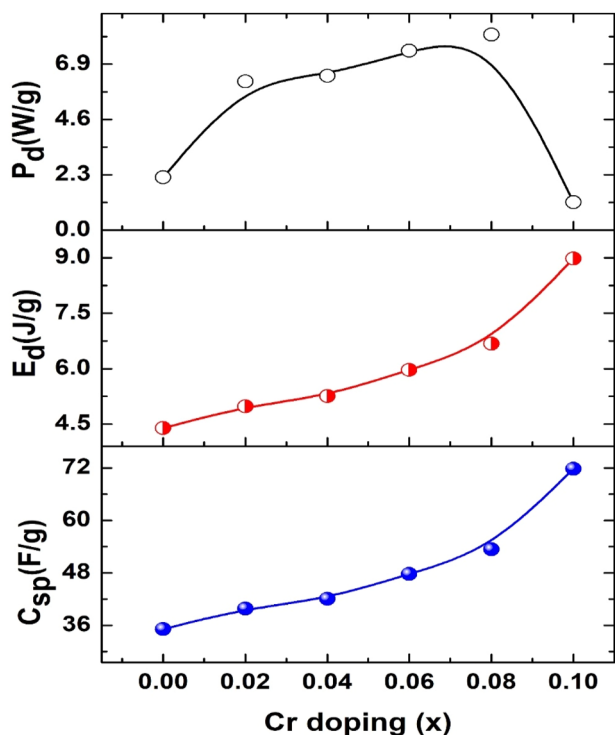
Fig. 13 The variation of specific-capacitance (C_{sp}), Energy density (E_d) and power density (P_d) with respect to dopant x

The potential versus time curves exhibit the pseudocapacitive characteristics of the electrode. Table 2 shows the values of specific capacitance (C_{sp}), energy density (E_d), and power density (P_d) at a scan rate of 5 mV/s for all the samples. The variation of C_{sp}, E_d, and P_d with doping concentration, x, is shown in Fig. 13. It is observed from Fig. 13a that C_{sp} increased with doping concentration, x. A similar variation is observed for E_d with x. It is observed that C_{sp} is 70.286 F/g, for $x = 0.0$ and 143.671 F/g for $x = 0.10$. The Cr^{3+} doped samples exhibit greater C_{sp} as compared to $ZnAl_2O_4$ ($x = 0.0$) which may be due to the larger electrochemical surface area. Mukhtiar Hussain et al. reported a specific capacitance of 1194.69 Fg^{-1} for Nd-doped $FeAl_2O_4$ nanoparticles subjected to a current density of 1.0 Ag^{-1} [59]. Salma Aman et al. synthesized $SrAl_2O_4$

using the hydrothermal route. It is reported that $SrAl_2O_4$ exhibited a large specific capacitance of 737 Fg^{-1} at 1 Ag^{-1} [60]. The $NiCo_2O_4$ prepared using oxalic acid showed a specific capacitance of 1254 Fg^{-1} at 2 Ag^{-1} [61]. The $ZnAl_2O_4$ electrode material showed a specific capacity of 255.4 $mAhg^{-1}$ at the current density of 1 Ag^{-1} elsewhere [25]. There is a linear variation in the energy density from $x = 0.0$ (2.439 Wh/kg) to $x = 0.10$ (4.987 Wh/kg). The power density increased from 15.790 W/kg ($x = 0.0$) to 58.546 W/kg ($x = 0.08$) and decreased to 8.537 W/kg at $x = 0.10$.

4 Conclusions

The Cr doped $ZnAl_2O_4$ samples were prepared using microwave hydrothermal method at 200 °C/60 min. The cubic structure of the spinel was confirmed by XRD. The lattice constant (a) increased from 8.085 Å ($x = 0.0$) to 8.128 Å ($x = 0.04$) and decreased to 8.104 Å ($x = 0.10$) with Cr doping. The changes in lattice constant, a, is explained on the basis of ionic radii. The differing molar masses of Zn (65.4 g/mol), Al (27 g/mol), and Cr (51.996 g/mol) explain the difference in d_x with respect to x. The average grain size is estimated to be between 84 nm ($x = 0.0$) and 198 nm ($x = 0.10$). Three absorption bands were detected at about 649 cm^{-1}, 544 cm^{-1}, and 497 cm^{-1} for sample $x = 0.0$, indicating the formation of the spinel cubic phase. The band gap energy for $x = 0.0$ is 3.51 eV, which is less than the band gap of bulk $ZnAl_2O_4$ (3.8 eV). The energy band gap (E_g) decreased from 3.51 eV ($x = 0.0$) to 3.39 eV ($x = 0.10$) with doping. The XPS confirms the presence of Cr, Al, Zn and O in respective valence states. The O 1 s spectra confirms the oxygen defects in the doped samples. The maximum specific capacitance (C_{sp}) of 143.671 F/g, is obtained for $x = 0.1$. The Cr^{3+}-doped samples have higher C_{sp} than $ZnAl_2O_4$ ($x = 0.0$) due to their larger electrochemical surface area. Therefore, the chromium doped $ZnAl_2O_4$ may be useful for energy storage supercapacitors.

Compliance with ethical standards

References

1. Frackowiak E, Abbas Q, Béguin F (2013) Carbon/carbon supercapacitors. J Energy Chem 22:226–240

2. Wang G, Zhang L, Zhang J (2011) A review of electrode materials for electrochemical supercapacitors. Chem Soc Rev 41:797–828

3. Raj BGS, Asiri AM, Qusti AH, Wu JJ, Anandan S (2014) Sonochemically synthesized MnO_2 nanoparticles as electrode material for supercapacitors. Ultra Sonochem 21:1933–1938

4. Srither R, Karthik A, Arunmetha S, Murugesan D, Rajendran V (2016) Electrochemical supercapacitor studies of porous MnO2 nanoparticles in neutral electrolytes. Mater Chem Phys 183:375–382

5. Interrante LV, Hampden-Smith MJ (1998) Chemistry of Advanced Materials: an Overview. Wiley VCH, New York

6. Xiaoyan G, Jiancheng D (2007) Preparation and electrochemical performance of nano-scale nickel hydroxide with different shapes. Mater Lett 61:621–625

7. Uberuaga BP, Bacorisen D, Smith R, Ball JA, Grimes RW, Voter AF, Sickafus KE (2007) Phys Rev B 75:104–116

8. do Nascimento NMP, de Lima BRM, Zamian JR, da Costa CEF, do Nascimento LAS, Luque R, da Rocha Filho GN (2020) Synthesis of Mesoporous $Zn_{1-x}M_xAl_2O_4$ Substituted by Co^{2+} and Ni^{2+} Ions and Application in the Photodegradation of Rhodamine B. Mater 13(9):2150

9. Battiston S, Rigo C, daCruz E, Severo, Mazutti MA, Kuhn RC, Gündel A, Foletto MA (2014) Synthesis of zinc aluminate (ZnAl2O4) spinel and its application as photocatalyst. Mater Res 17:734–738

10. Lahmer MA (2019) The effect of Fe-doping on the electronic, optical and magnetic properties of ZnAl2O4; a first-principles study. Comput Condens Matter 20:e00387

11. Einbergs E, Zolotarjovs A, Bite I, Laganovska K, Auzins K, Smits K, Trinkler K (2019) Usability of Cr-doped alumina in dosimetry. Ceramics 2:525–535

12. Sampath SK, Kanhere DG, Pandey R (1999) Electronic structure of spinel oxides: zinc aluminate and zinc gallate. J Phys Condens Matter 11:3635–3644

13. Le Nestour A, Gaudon M, Villeneuve G, Daturi M, Andriessen R, Demourgues A (2007) Defects in divided zinc-copper aluminate spinels: structural features and optical absorption properties. Inorg Chem 46:4067–4078

14. Thirumala Rao G, Babu B, Kim J, Yoo K (2022) Efficient photoelectrochemical water oxidation and electrochemical supercapacitor performance of ZnAl2O4 hexagonal microstructures. Mater Lett 313:131812

15. Rojas-Hernandez RE, Rubio-Marcos F, Rezende MV, Rodriguez MÁ, Serrano A, Muñoz-Noval Á, Fernandez JF (2016) The impact of the synthesis conditions on SrAl 2 O 4 :Eu, Dy formation for a persistent afterglow. Mater Des 108:354–363

16. Fernández-Osorio A, Rivera CE, Vázquez-Olmos A, Chávez J (2015) Luminescent ceramic nano-pigments based on terbium-doped zinc aluminate: Synthesis, properties and performance. Dyes Pigments 119:22–29

17. Prusty RK, Kuruva P, Ramamurty U, Thomas T (2013) Correlations between mechanical and photoluminescence properties in Eu doped sodium bismuth titanate. Solid State Commun 173:38–41

18. Tshabalala KG, Cho SH, Park JK, Pitale SS, Nagpure IM, Kroon RE, Swart HC, Ntwaeaborwa OM (2011) Luminescent properties and X-ray photoelectron spectroscopy study of ZnAl2O4:-Ce3+,Tb3+ phosphor. J Alloy Comp 509:10115–10120

19. Menon SG, Hebbar DN, Kulkarni SD, Choudhari K, Santhosh C (2017) Neuropeptides: A promising target for treating seizures. Mater Res Bull 86:63–71

20. Sampath SK, Cordaro JF (1998) Optical Properties of Zinc Aluminate, Zinc Gallate, and Zinc Aluminogallate Spinels. J Am Ceram Soc 81:649–654

21. Matsui H, Xu CN, Tateyama H (2001) Stress-stimulated luminescence from ZnAl2O4:Mn. Appl Phys Lett 78:1068–1070

22. Zawadzki M (2006) Synthesis of nanosized andmicroporous zinc aluminate spinel by microwave assisted hydrothermal method(microwave–hydrothermal synthesis of $ZnAl_2O_4$ Solid State Sci 8:14–18

23. Yang CC, Chen SY, Cheng SY (2004) Laquinimod (ABR-215062) suppresses the development of experimental autoimmune encephalomyelitis, modulates the Th1/Th2 balance and induces the Th3 cytokine TGF-beta in Lewis rats. Powder Technol 148:3–6

24. Duan X, Yuan D, Wang X, Xu H (2005) Synthesis and characterization of nanocrystalline zinc aluminum spinel by a new sol-gel method. J Sol-Gel Sci Technol 35:221–224

25. Duan X, Yuan D, Sun Z, Luan C, Pan D, Xu D (2005) Preparation of Co2+-doped ZnAl2O4 nanoparticles by citrate sol–gel method. J Alloy Compd 386:311–314

26. Basavaraju N, Priolkar KR, Gourier D, Sharma SK, Bessière A, Viana B (2015) The importance of inversion disorder in the visible light induced persistent luminescence in Cr^{3+} doped AB_2O_4 (A = Zn or Mg and B = Ga or Al). Phys Chem Chem Phys 17:1790–1799

27. Patil KC, Hegde MS, Rattan T, Aruna ST (2008) Chemistry of nanocrystalline oxide materials: combustion synthesis, properties and applications. World Scientific

28. Miron I, Grozescu I (2012) Optoelectron Adv Mater Rapid Commun 6:673–675

29. Lanh PT, Long NN, Loan TT (2009) Some physical properties of ZnAl2O4: Cr3+(Co2+) powders prepared by hydrothermal method. J Phys Conf Ser 187(1):012053

30. Motloung S, Dejene F, Ntwaeaborwa O, Swart H (2014) Effects of catalyst/zinc mole fraction on ZnAl2O4:0.01% Cr3+nanocrystals synthesized using sol–gel process. Mater Res Express 1(4):045029

31. Dong G, Xiao X, Peng M, Ma Z, Ye S, Chen D, Qin H, Deng G, Liang Q, Qiu J (2012) RSC Adv 2:2773–2782

32. Sadhana K, Praveena K, Matteppanavar S, Angadi B (2012) Structural and magnetic properties of nanocrystalline BaFe12O19 synthesized by microwave-hydrothermal method. Appl Nanosci 2(3):247–252

33. Katlakunta S, Meena SS, Srinath S, Bououdina M, Sandhya R, Praveena K (2015) Improved magnetic properties of Cr3+ doped SrFe12O19 synthesized via microwave hydrothermal route. Mater Res Bull 63:58–66

34. Cheng B, Qu S, Zhou H, Wang Z (2006) Porous ZnAl2O4spinel nanorods doped with Eu3+: synthesis and photoluminescence. Nanotechnology 17:2982–2987

35. Ahmed MA, El-Dek SI, El-Kashef IM, Helmy N (2011) Structural and magnetic properties of nano-crystalline Ag+ doped NiFe2O4. Solid State Sci 13:1176–1179

36. Rathod V, Anupama AV, Vijaya Kumar R, Jali VM, Sahoo B (2017) Correlated vibrations of the tetrahedral and octahedral complexes and splitting of the absorption bands in FTIR spectra of Li-Zn ferrites. Vibrational Spec 92:267–272

37. Huang S-P, Wei Z-Q, Wu X-J, Shi J-W (2020) Sputtering parameters effect on microstructural parameters of TiN coating via the Williamson-Hall analysis. Mater Res Express 7:015025–015025(10)

38. Abdurakhmonova OE, Alisultanova ME, Vertaevaa DA, Muradovaa AG (2022) The effect of annealing temperature on crystallization of Nd2O3 nanoparticles synthesized by the deposition method. Russ J Inorg Chem 67:1118–1124

39. Abdul W, Abdullah AM, Mohammed Rahman M (2019) One-step facile synthesis of Nd2O3/ZnO nanostructures for an efficient selective 2,4-dinitrophenol sensor probe. Appl Sur Sci 487:1253–1261

40. Ge DL, Fan YJ, Qi CL, Sun ZX (2013) Facile synthesis of highly thermostable mesoporous ZnAl2O4with adjustable pore size. J Mater Chem A 1(5):1651–1658

41. Mathur S, Veith M, Haas M, Shen H, Lecerf N, Huch V, Hüfner S, Haberkorn R, Beck HP, Jilavi M (2010) Single-source sol-gel

synthesis of nanocrystalline ZnAl2O4: structural and optical properties. J Am Ceram Soc 84:1921–1928

42. Kumar S, Song T, Gautam S, Chae K, Kim S, Jang K (2015) Structural, magnetic and electronic structure properties of Co doped ZnO nanoparticles. Mater Res Bull 66:76–82

43. Japic D, Bitenc M, Arinsek M, Orel ZC (2014) The impact of nano-milling on porous ZnO prepared from layered zinc hydroxide nitrate and zinc hydroxide carbonate. Mater Res Bull 60:738–745

44. McMillan P, Piriou B (1982) The structures and vibrational spectra of crystals and glasses in the silica-alumina system. J Non-Cryst Solids 53:279–298

45. Preudhomme J, Tarte P (1971) Spectrochim acta part. A Mol Spectrosc 27:1817–1835

46. Mazza D, Vallino M, Busca G (1992) Mullite-type structures in the systems Al2O3–Me2O (Me = Na, K) and Al2O3–B2O3. J Am Ceram Soc 75:1929–1934

47. Hoffmann HR, Martin ST, Choi W, Bahnemann DW (1995) Environmental applications of semiconductor photocatalysis. Chem Rev 95:69–96

48. Cullity BD (1956) Elements of X-ray Diffraction, 2nd Edn. Addison Wesley, Reading, MA, p 285

49. Weckhuysen BM, Verberckmoes AA, De Baets AR, Schoonheydt RA (1997) Diffuse reflectance spectroscopy of supported chromium oxide catalysts: A self-modeling mixture analysis. J Catal 166:160–171

50. Singh AK, Nakate U (2013) Microwave synthesis, characterization and photocatalytic properties of SnO2 nanoparticles. Adv Nanopart 2:66–70

51. Pailhe N, Wattiaux A, Gaudon M, Demourgues A (2008) Correlation between structural features and vis–NIR spectra of α-Fe2O3 hematite and AFe2O4 spineloxides (A=Mg, Zn J Solid State Chem 181(5):1040–1047

52. Nie W, Michel-Calendini FM, Linares C, Boulon G (1990) New results on optical properties and term-energy calculations in Cr3+-doped ZnAl2O4. J Lumin 46:177–190

53. Dhamale GD, Mathe VL, Bhoraskar SV, Sahasrabudhe SN, Dhole SD, Ghorui S (2016) Synthesis and characterization of Nd2O3-nanoparticles in a radiofrequency thermal plasma reactor. Nanotechnology 27(8):085603(1)–085603(9)

54. Strohmeier BR (1994) Zinc Aluminate (ZnAl2O4) by XPS. Surf Sci Spectra 3(2):128–134

55. Basyooni A, Emese K, Walid B, Irina H, István K (2023) Role of A-site (Sr), B-site (Y), and A, B sites (Sr, Y) substitution in lead-free BaTiO3 ceramic compounds: Structural, optical, microstructure, mechanical, and thermal conductivity properties. Ceram Int 49(2):1947–1959

56. Li LZ, Ding Z, He Y (2017) Ultrafine Nd 2 O 3 nanoparticles doped carbon aerogel to immobilize sulfur for high performance lithium–sulfur batteries. J Electroanal Chem 799:617–624

57. Angelin MD, Rajkumar S, Merlin JP, Xavier AR, Franklin M, Ravichandran A (2020) Electrochemical investigation of Zr-doped ZnO nanostructured electrode material for high-performance supercapacitor. Ionics 26:5757–5772

58. Zhang H, Gu J, Tong J, Hu Y, Guan B, Hu B, Zhao J, Wang C (2016) Hierarchical porous MnO 2 /CeO 2 with high performance for supercapacitor electrodes. J Chem Eng 286:139–149

59. Mukhtiar H, Alanazi MM, Abdelmohsen SAM, Abdullah M, Ali M, Aman S, Al-Sehemi AG, Henaish AMA, Farid HMT (2024) Enhanced Supercapacitive Performance of FeAl2O4 Nanoparticles with Neodymium (Nd) Doping by Sonication Method. JOM 76:3185–3194

60. Aman S, Gouadria S, Alharbi FF, Saeed MN, Farid HM (2023) Novel Sr-based Al2O4 spinel material an environmental friendly electrode for supercapacitor application. Appl Phys A 129(5):347

61. Irong Z, Ji X, Wu Z, Song W, Hou H, Wu Z, He X, Chen Q, Craig E (2014) Spinel NiCo2O4 for use as a high-performance supercapacitor electrode material: Understanding of its electrochemical properties. J Power Sources 267:888–900